A new Algorithm for Flaw Simulation in Castings by Superimposing Projections of 3D Models onto X-Ray Images

Domingo Mery
Department of Computer Engineering
University of Santiago of Chile
Av. Ecuador 3659, Santiago de Chile
dmery@ieee.org
www.diinf.usach.cl/∼dmery

Abstract

In order to evaluate the sensitivity of defect inspection systems, it is convenient to examine simulated data. This gives the possibility to tune the parameters of the inspection method and to test the performance of the system in critical cases. In this paper, a simple method for the simulation of defects in radioscopic images of aluminum castings is presented. The approach simulates only the flaws and not the whole radioscopic image of the object under test. A 3D flaw is modeled as an ellipsoidal cavity, which is projected and superimposed onto real radioscopic images of an homogeneous object according to the exponential attenuation law for x-rays. The new gray value of a pixel, where the 3D flaw is projected, depends only on four parameters: a) the original gray value; b) the linear absorption coefficient of the examined material; c) the maximal thickness observable in the radioscopic image; and d) the length of the intersection of the 3D flaw with the modeled x-ray beam, that is projected into the pixel. A simulation of an ellipsoidal flaw of any size and orientation can be done in any position of the casting by using the algorithm described in this paper. This allows the evaluation of the performance of defect inspection systems in cases where the detection is known to be difficult.

1 Introduction

Radioscopy is increasingly being used as a tool for nondestructive testing in industrial production. An example is the serial examination of cast light-alloy workpieces used in the car industry, like aluminum wheels and steering gears [12]. The material defects occurring in the casting process such as cavities, gas, inclusions, and sponging must be detected to satisfy the safety requirements; consequently, it is necessary to check 100% of the parts. Since most defects are not visible, x-ray imaging is used for this task. An example of a radioscopic image is shown in Figure 1.

Over the past decades radioscopic systems have been introduced in the automotive manufacturing industry in order to detect flaws automatically without human interaction [1, 5, 11]. Over the years, they have not only increased quality through repeated objective inspections and improved processes, but have also increased productivity through decreased labor cost [16, 14].

An automated radioscopic system is schematically presented in Figure 2. The inspection is typically performed in the five following steps: *i)* the *manipulator* places the casting in the desired position; *ii)* the *x-ray tube* generates an x-ray image of the casting via central projection; *iii)* the x-ray image is detected by the fluorescent entrance screen of the *image intensifier*, amplified and depicted onto a phos-

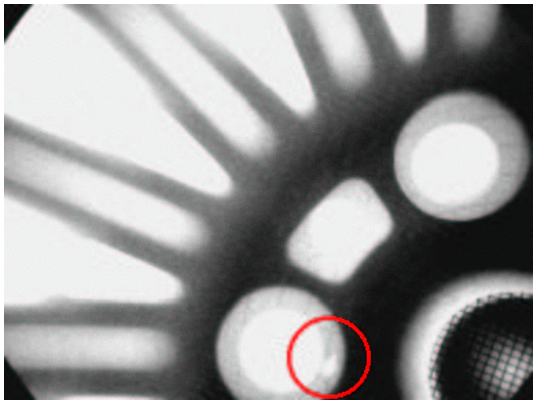

Figure 1. A real flaw in a radioscopic image of an aluminum wheel.

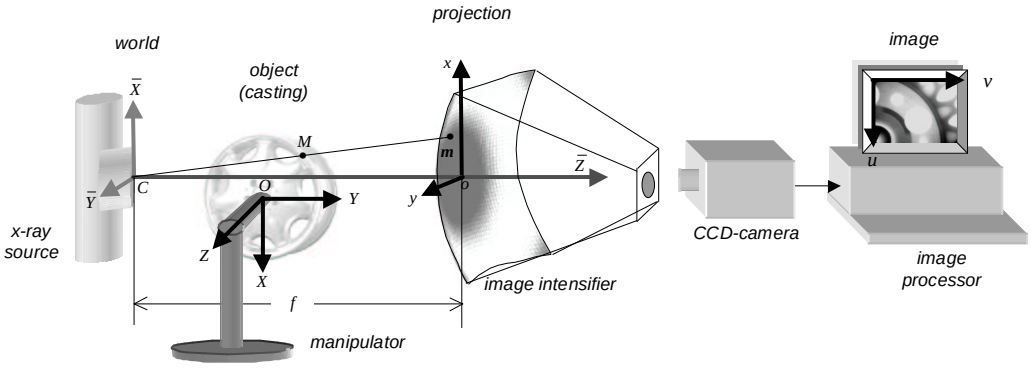

Figure 2. Diagram of a radioscopic imaging system.

phor screen. The image intensifier converts the x-ray image to a visible radioscopic image; *iv)* the guided and focussed image is registered by the *CCD-camera*; and *v)* the *image processor* converts the analog video signal, transferred by the CCD-camera, into a digital data stream. Digital image processing is used to improve and evaluate the radioscopic image.

In order to evaluate the performance of a method that inspects aluminum castings, it is convenient to examine simulated data. This evaluation gives the possibility of tuning the parameters of the inspection method and of testing how the method works in critical cases. Among the nondestructive testing and evaluation community there are two widespread approaches that produce this simulated data: *flaw superimposition* and *CAD models for casting and flaw*.

Flaw superimposition. The first technique attempts to simulate flaws by superimposing circles with different gray values onto real radioscopic images [11, 10, 5]. This approach is quite simple, because it does not need any complex 3D model of the object under test nor of the flaw. Additionally, it offers a real radioscopic image with real disturbances (with simulated flaws). Nevertheless, the flaws simulated by this method differ significantly from the real ones. The reason being that a real flaw does not look like a projection of a disc. This method can only be used in restricted cases.

An improvement of this method can be obtained using the visualization technique called *splatting* [20]. In this technique the projection of a 3D flaw can be simulated, in which the projected flaw is assumed as a 2D Gaussian. The scale, position and orientation of the Gaussian are adjusted in order to obtain the desired projected flaw. Although this technique offers a better flaw simulation in comparison with the disc projection, its simulation corresponds to the projection of a 3D flaw, that differs considerably from real flaws as shown later.

CAD models for casting and flaw. The second approach makes a simulation of the entire x-ray imaging process [18, 6]. In this approach, the characteristic of the x-ray source, the geometry and material properties of objects and their defects, as well as the imaging process itself are modeled and simulated independently. Complex objects and defect shapes can be simulated using CAD models. Although this approach offers excellent flexibility in setting the objects and flaws to be tested, it presents the following three disadvantages to the evaluation of the inspection methods' performance: *i)* the radioscopic image of the object under test is simulated (it would be better if we could count on real images with simulated flaws); *ii)* the simulation approach is only available when using a sophisticated computer package; *iii)* the computing time is expensive.

In this paper, we address the above problems and propose an approach that only simulates the flaws (and not the whole radioscopic image of the object under test). This new method can be viewed as an improvement of the first mentioned technique and the 3D modeling for the flaws of the second one. In our approach, a 3D modeled flaw is projected and superimposed onto real radioscopic images of a homogeneous object according to the exponential attenuation law for x-rays [7]. We propose an ellipsoidal model to simulate the flaws. This model suits best reality for flaws like bubbles and spherical blowholes. The methodology used in this paper can be used for other 3D models.

The paper is organized as follows: In Section 2, a brief overview of the x-ray imaging process is presented. Section 3 describes our geometric model of the x-ray projection. The approach to simulate flaws in aluminum castings is outlined in Section 4. The results obtained on radioscopic images are described in Section 5. Finally, Section 6 gives concluding remarks and suggestions for future research.

2 X-Ray Imaging

Radiographic examination is a nondestructive testing technique which uses x-ray radiation to detect material defects. In this examination method, radiation is passed through the material under test, and a detector senses the radiation intensity attenuated by the material. Thus, a defect in the material modifies the expected radiation received by the sensor [8]. The phenomenon of differential absorption is illustrated in Figure 3. The contrast in the x-ray image between an area containing a flaw and a defect-free area of the specimen allows distinguishing the flaw. We can see in an x-ray image, that the defects, like voids, cracks or bubbles, show up as bright regions with respect to their neighboring area. The reason is that the attenuation is smaller.

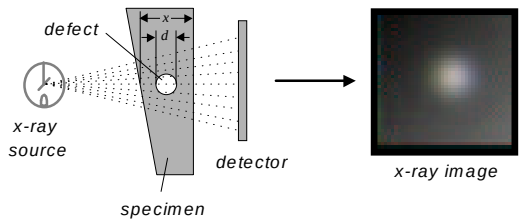

Figure 3. Differential absorption in a specimen.

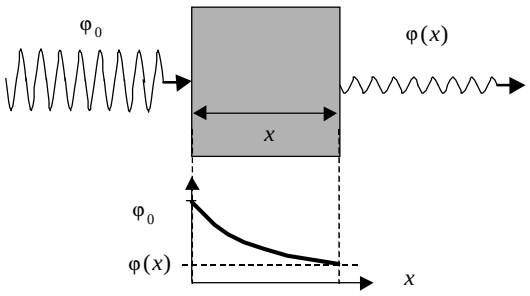

Figure 4. Absorption law.

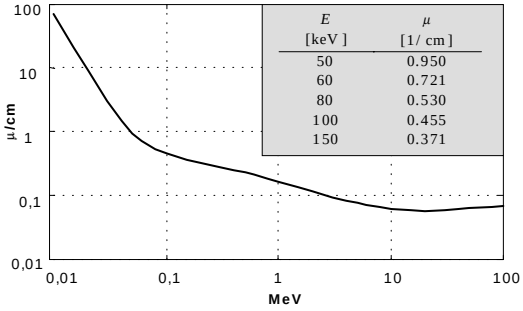

Figure 5. Absorption coefficient μ for aluminum against x-ray energy [13, 10].

The absorption can be macroscopically modeled using the exponential attenuation law for x-rays [8, 7] as shown in Figure 4:

$$\varphi(x) = \varphi_0 e^{-\mu x}, \tag{1}$$

where φ_0 is the incident radiation intensity, φ the transmitted intensity, x the thickness of the specimen and μ is a constant known as the *linear absorption coefficient* of the material under test with dimension cm^{-1}. Coefficient μ depends on the material and the x-ray energy. Figure 5 illustrates the linear absorption coefficient for aluminum plotted against x-ray energy. Typically, radioscopic testing of aluminum castings uses energy values between 50keV and 150keV [10]. In Figure 5, the reader can find the values of μ for this energy interval, in which μ can be modeled as a fourth degree polynomial:

$$\mu \approx \sum_{i=0}^{4} \theta_i E^i \quad \text{for} \quad 50\text{keV} \leq E \leq 150\text{keV}, \tag{2}$$

with

$$\theta = (6.0, -0.210, -0.00304, -1.97 \times 10^{-5}, 4.72 \times 10^{-8}).$$

The gray value I registered by the CCD-camera can be expressed as a linear function of φ:

$$I(x) = A\varphi(x) + B, \tag{3}$$

where A and B are the linear parameters of I.

Now, we investigate what happens if the penetrated object has a cavity with thickness d as shown in Figure 3. In this case, from (1) the transmitted radiation φ_d is given by:

$$\varphi_d = \varphi(x-d) = \varphi_0 e^{-\mu(x-d)} = \varphi(x) e^{\mu d}, \tag{4}$$

where we assume that the absorption coefficient of the cavity is zero[1].

The gray value registered by the CCD camera is calculated then from (4) and (3) as:

$$I(x-d) = A\varphi(x)e^{\mu d} + B. \tag{5}$$

Substituting the value of $A\varphi(x)$ from (3) we see that (5) may be written as:

$$I(x-d) = (I(x) - B)e^{\mu d} + B. \tag{6}$$

Parameter B can be estimated as follows: the maximal gray value I_{max} in a radioscopic image is obtained when

[1] If the flaw is an incrusted material, its absorption coefficient μ_d must be considered in (4): $\varphi_d = \varphi_0 e^{-\mu(x-d)} e^{-\mu_d d} = \varphi(x) e^{d(\mu-\mu_d)}$.

the thickness is zero. Additionally, the minimal gray value I_{min} is obtained when the thickness is x_{max}. Substituting these values in (3), it yields:

$$\begin{cases} I_{max} &= A\varphi_0 + B \\ I_{min} &= A\varphi_0 e^{-\mu x_{max}} + B \end{cases}$$

From these equations, we obtain that:

$$B = I_{max} - \Delta I/(1 - e^{-\mu x_{max}}) \ , \qquad (7)$$

where $\Delta I = I_{max} - I_{min}$. Usually, I_{max} and I_{min} are 255 and 0 respectively. For these values, B can be written as:

$$B = 255/(1 - e^{\mu x_{max}}) \ . \qquad (8)$$

Using equation (6), we can alter the original gray value of the radioscopic image $I(x)$ to simulate a new image $I(x - d)$ with a flaw. A 3D flaw can be modeled, projected and superimposed onto a real radioscopic image. The new gray value of a pixel, where the 3D flaw is projected, depends only on four parameters: a) the original gray value $I(x)$; b) the linear absorption coefficient of the examined material μ; c) the maximal thickness observable in the radioscopic image x_{max}; and d) the length of the intersection of the 3D flaw with the modeled x-ray beam d, that is projected into the pixel. In the next Section we will describe how a 3D object is projected onto a radioscopic image.

3 Geometric Model

In this Section a model is presented which relates the 3D coordinates of the casting (from now on *object*) to the 2D coordinates of the radioscopic image pixel.

One can define the following coordinate systems to describe the relationship between a 3D object point and a 2D pixel, as shown in Figure 2:

• The 3D **object coordinate system** is attached to the object. An object point M in this coordinate system is denoted by $\mathbf{M} = [X\ Y\ Z\ 1]^\mathsf{T}$ in projective coordinates [9, 4]. The origin of this coordinate system is denoted by O.

• The 3D **world coordinate system** is defined in the optical center of the central projection, i.e. its origin C corresponds to the x-ray source. The object point M in this coordinate system is $\bar{\mathbf{M}} = [\bar{X}\ \bar{Y}\ \bar{Z}\ 1]^\mathsf{T}$ in projective coordinates. The object coordinate system is then considered as a rigid displacement of the world coordinate system represented by a 3×3 rotation matrix $\mathbf{R}$ and a 3×1 translation vector $\mathbf{t}$ [4]. With the 4×4 matrix $\mathbf{S}$:

$$\mathbf{S} = \begin{bmatrix} \mathbf{R} & \mathbf{t} \\ \mathbf{0} & 1 \end{bmatrix}, \qquad (9)$$

one obtains the relationship between object and world coordinate system:

$$\bar{\mathbf{M}} = \mathbf{SM}. \qquad (10)$$

• A 2D **projection coordinate system** is then defined. This coordinate system indicates the coordinates of a point in the (not visible) x-ray image at a imaginary plane $\bar{Z} = f$ located at the entrance screen of the image intensifier. Its origin o is pierced by the $\bar{Z}$-axis. The x-rays make a linear perspective projection of the point M onto a point m in the imaginary plane without any distortion. Applying Thales theorem:

$$\frac{x}{f} = \frac{\bar{X}}{\bar{Z}} \quad \text{and} \quad \frac{y}{f} = \frac{\bar{Y}}{\bar{Z}}, \qquad (11)$$

the projective coordinates of m in this 2D system can be obtained as $\mathbf{m} = [x\ y\ 1]^\mathsf{T}$. Using $\bar{\mathbf{M}}$ and $\mathbf{m}$ as projective representations of M and m respectively, the following linear equation is obtained:

$$\lambda \mathbf{m} = \underbrace{\begin{bmatrix} f & 0 & 0 & 0 \\ 0 & f & 0 & 0 \\ 0 & 0 & 1 & 0 \end{bmatrix}}_{\mathbf{B}} \bar{\mathbf{M}}, \qquad (12)$$

where λ is a scale factor. One may denote by $\mathbf{P} = \mathbf{BS}$ the 3×4 perspective projection matrix. From (10) and (12) one obtains the equation that maps the object coordinates to the projection plane coordinates:

$$\lambda \mathbf{m} = \mathbf{PM}. \qquad (13)$$

• Finally, the 2D **image coordinate system** is introduced as a representation of the pixel coordinates of the (visible) radioscopic image formed at the CCD camera. The point $\mathbf{m}$ is projected onto the plane of the CCD-array as $\mathbf{u} = [u\ v\ 1]^\mathsf{T}$

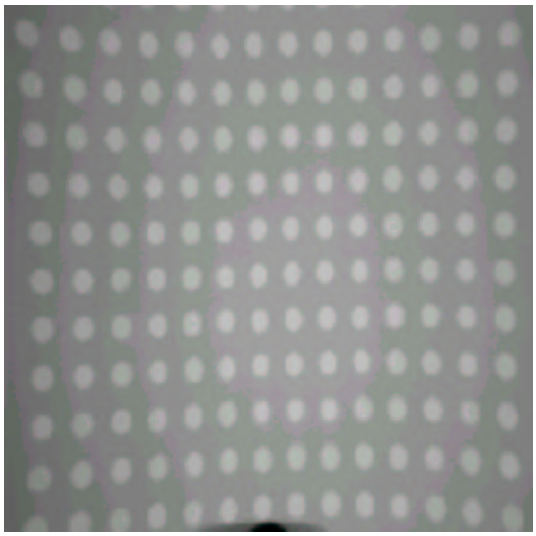

Figure 6. Radioscopic image of a plate with holes distributed in a regular grid manner.

in projective coordinates. Due to the curvature of the entrance screen of the image intensifier and the electromagnetic fields that may be present in the radioscopic system, the radioscopic image received by the CCD camera is deformed, especially at the corners of the image. Therefore, the relationship between the projection and the image coordinate system is nonlinear:

$$\mathbf{u} = \mathbf{f}(\mathbf{m}). \tag{14}$$

The nonlinear function $\mathbf{f}$ can be modeled as hyperbolic [15, 14], cubic [2] or by a general distortion model [19]. This function can be estimated by analyzing the projective distortion of a calibration plate which contains holes placed in a regular grid manner. The phenomenon of the distortion effect is illustrated in Figure 6, where a radioscopic image of a calibration plate is shown.

From (13) and (14) a relation can be made between the 3D coordinates of the object and the radioscopic image pixel coordinates at each position of the object.

In the following Section we use this geometric model to simulate the projection of a modeled 3D flaw into a real radioscopic image.

4 Simulation of Flaws

In this paper, a 3D flaw is simulated as a blowhole with a spherical form. We propose an ellipsoidal model to simulate the flaws, because this model suits best reality for flaws like bubbles. The surface of the ellipsoid is given by:

$$\frac{X'^2}{a^2} + \frac{Y'^2}{b^2} + \frac{Z'^2}{c^2} = 1, \tag{15}$$

where a, b and c are the ellipsoid half-axes as shown in Figure 7. The axes X', Y' and Z' are attached to the center of the ellipsoid. The location of the ellipsoid relative to the object coordinate system is defined by a 3×3 rotation matrix $\mathbf{R}_e$ and a 3×1 translation vector $\mathbf{t}_e$. They can be arranged in a 4×4 matrix $\mathbf{S}_e$ as in equation (9). Using (10), the coordinates in the ellipsoid coordinate system (X', Y', Z') can be expressed in the world coordinate system $(\bar{X}, \bar{Y}, \bar{Z})$ as:

$$\bar{\mathbf{M}} = \mathbf{S}\mathbf{M} = \mathbf{S}\mathbf{S}_e\mathbf{M}', \tag{16}$$

with $\mathbf{M}' = [X'\ Y'\ Z'\ 1]^\mathsf{T}$ and $\bar{\mathbf{M}} = [\bar{X}\ \bar{Y}\ \bar{Z}\ 1]^\mathsf{T}$. Now, we can write the equation of the ellipsoid in world coordinate system from (15) and (16) as:

$$\begin{array}{rcl} (h_{11}\bar{X} + h_{12}\bar{Y} + h_{13}\bar{Z} + h_{14})^2/a^2 & + & \\ (h_{21}\bar{X} + h_{22}\bar{Y} + h_{23}\bar{Z} + h_{24})^2/b^2 & + & \\ (h_{31}\bar{X} + h_{32}\bar{Y} + h_{33}\bar{Z} + h_{34})^2/c^2 & = & 1 \end{array}, \tag{17}$$

where h_{ij} are the elements of the 4×4 matrix $\mathbf{H} = [\mathbf{S}\mathbf{S}_e]^{-1}$.

Suppose that we have a pixel (u, v) of a radioscopic image and we want to know if the x-ray beam, which produces a gray value in this pixel, intersects the modeled ellipsoid. Using the inverse function of $\mathbf{f}$ in (14) we can calculate the corresponding coordinates of (u, v) in the projection coordinate systems (x, y):

$$\mathbf{m} = \mathbf{g}(\mathbf{u}) = \mathbf{f}^{-1}(\mathbf{u}), \tag{18}$$

with $\mathbf{u} = [u\ v\ 1]^\mathsf{T}$ and $\mathbf{m} = [x\ y\ 1]^\mathsf{T}$. The x-ray beam in the world coordinate system is defined in (11). The intersection of the x-ray beam with the ellipsoid is shown in Figure 8. An intersection point must satisfy (17) and (11) simultaneously. Substituting $\bar{X} = x\bar{Z}/f$ and $\bar{Y} = y\bar{Z}/f$ from (11) in (17) and after some manipulation we obtain:

$$A\bar{Z}^2 + B\bar{Z} + C = 0,$$

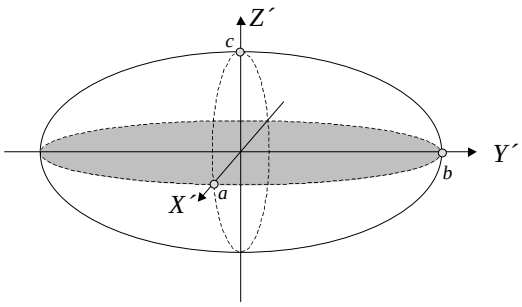

Figure 7. Ellipsoid used as 3D flaw.

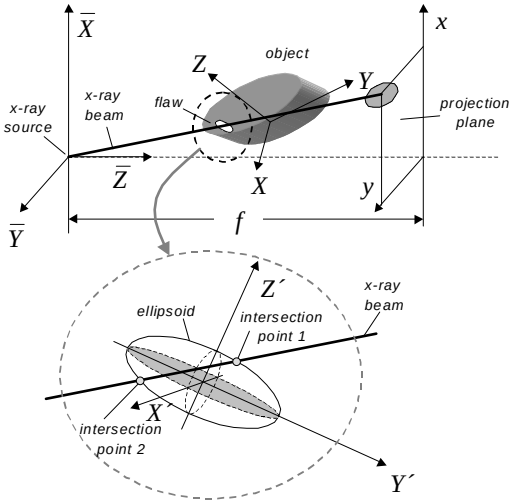

Figure 8. Intersection of an x-ray beam with the ellipsoid.

with

$$A = \frac{r_1^2}{a^2} + \frac{r_2^2}{b^2} + \frac{r_3^2}{c^2},$$

$$B = 2\left(\frac{r_1 h_{14}}{a^2} + \frac{r_2 h_{24}}{b^2} + \frac{r_3 h_{34}}{c^2}\right), \text{ and}$$

$$C = \frac{h_{14}^2}{a^2} + \frac{h_{24}^2}{b^2} + \frac{h_{34}^2}{c^2} - 1,$$

where

$$r_i = h_{i1}\frac{x}{f} + h_{i2}\frac{y}{f} + h_{i3} \qquad \text{for} \qquad i = 1, 2, 3.$$

If $B^2 - 4AC > 0$ there are two intersection points of the x-ray beam with the ellipsoid given by:

$$\bar{X}_{1,2} = \frac{\bar{Z}_{1,2}}{f} x$$

$$\bar{Y}_{1,2} = \frac{\bar{Z}_{1,2}}{f} y \tag{19}$$

$$\bar{Z}_{1,2} = \frac{-B \pm \sqrt{B^2 - 4AC}}{2A}$$

The length of the x-ray beam that penetrates into the ellipsoid can be calculated as:

$$d = \sqrt{(\bar{X}_1 - \bar{X}_2)^2 + (\bar{Y}_1 - \bar{Y}_2)^2 + (\bar{Z}_1 - \bar{Z}_2)^2},$$

that can be expressed from (19) as:

$$d = \frac{\sqrt{B^2 - 4AC}}{A}\sqrt{\frac{x^2}{f^2} + \frac{y^2}{f^2} + 1}. \tag{20}$$

Using matrix notation equation (20) can be rewritten as:

$$d = 2\frac{\sqrt{\bar{\mathbf{m}}^\mathsf{T}\mathbf{\Lambda}\bar{\mathbf{m}}}}{\bar{\mathbf{m}}^\mathsf{T}\mathbf{\Phi}\bar{\mathbf{m}}} \parallel \bar{\mathbf{m}} \parallel \tag{21}$$

with $\bar{\mathbf{m}} = [x/f \; y/f \; 1]^\mathsf{T}$,

$$\mathbf{\Lambda} = \mathbf{H}_s \mathbf{h}_d \mathbf{h}_d^\mathsf{T} \mathbf{H}_s^\mathsf{T} + (1 - \mathbf{h}_d^\mathsf{T}\mathbf{h}_d)\mathbf{\Phi}, \tag{22}$$

$$\mathbf{\Phi} = \mathbf{H}_s \mathbf{H}_s^\mathsf{T}, \tag{23}$$

where

$$\mathbf{H}_s = \begin{bmatrix} h_{11}/a & h_{21}/b & h_{31}/c \\ h_{12}/a & h_{22}/b & h_{32}/c \\ h_{13}/a & h_{23}/b & h_{33}/c \end{bmatrix}, \mathbf{h}_d = \begin{bmatrix} h_{14}/a \\ h_{24}/b \\ h_{34}/c \end{bmatrix}.$$

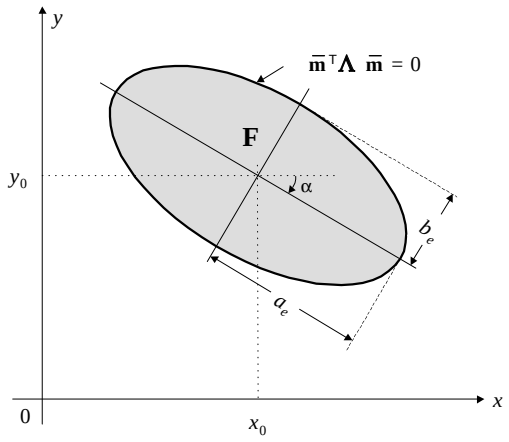

Figure 9. Area of the projected ellipsoid.

From (21) we observe that the projection of the ellipsoid is defined in the area (x, y) where

$$\bar{\mathbf{m}}^\mathsf{T}\mathbf{\Lambda}\bar{\mathbf{m}} > 0. \tag{24}$$

This area, denoted by $\mathbf{F}$ in Figure 9, is delimited by the boundary where $d = 0$, i.e. where $\bar{\mathbf{m}}^\mathsf{T}\mathbf{\Lambda}\bar{\mathbf{m}} = 0$. Due to the form of matrix $\mathbf{\Lambda}$ this equation corresponds to an ellipse [9].

Defining the upper left hand 2×2 matrix of $\mathbf{\Lambda}$:

$$\mathbf{A} = \begin{bmatrix} \Lambda_{11} & \Lambda_{12} \\ \Lambda_{21} & \Lambda_{22} \end{bmatrix}, \tag{25}$$

the coordinates of the center (x_0, y_0), the half-axes a_e and b_e and the orientation α of the ellipse (see Figure 9) can be computed as follows [3]:

$$\begin{bmatrix} x_0 \\ y_0 \end{bmatrix} = f\mathbf{A}^{-1}\begin{bmatrix} \Lambda_{13} \\ \Lambda_{23} \end{bmatrix}, \tag{26}$$

$$a_e = f\sqrt{-\tfrac{a_{00}}{\lambda_1}}, \quad b_e = f\sqrt{-\tfrac{a_{00}}{\lambda_2}} \tag{27}$$

and

$$\alpha = \arctan\left(\frac{C_{21}}{C_{11}}\right), \tag{28}$$

where $a_{00} = \det(\mathbf{\Lambda})/\det(\mathbf{A})$; λ_1, λ_2 are the eigenvalues from matrix $\mathbf{A}$; and C_{ij} are the elements of the 2×2 matrix $\mathbf{C}$ whose columns are the corresponding eigenvectors of $\mathbf{A}$.

An example can be found in Figure 10 in which the projection of an ellipsoid by computing (21) is illustrated. In Figure 10 the length d is plotted against x/f and y/f. We can see how abrupt is the change in d between the region $d > 0$ and its neighborhood. This feature is typical in real flaws like bubbles and spherical blowholes, because they are clearly delimited in the material [17]. The visualization

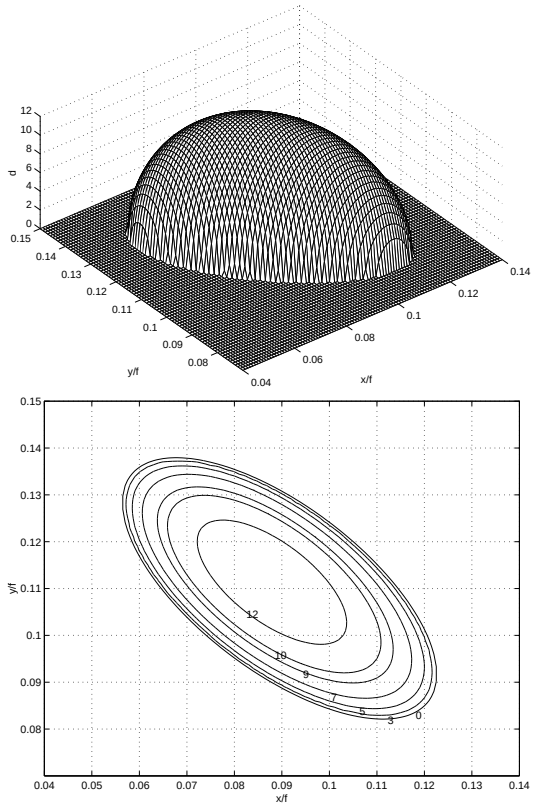

Figure 10. Projection of a flaw using an ellipsoidal model.

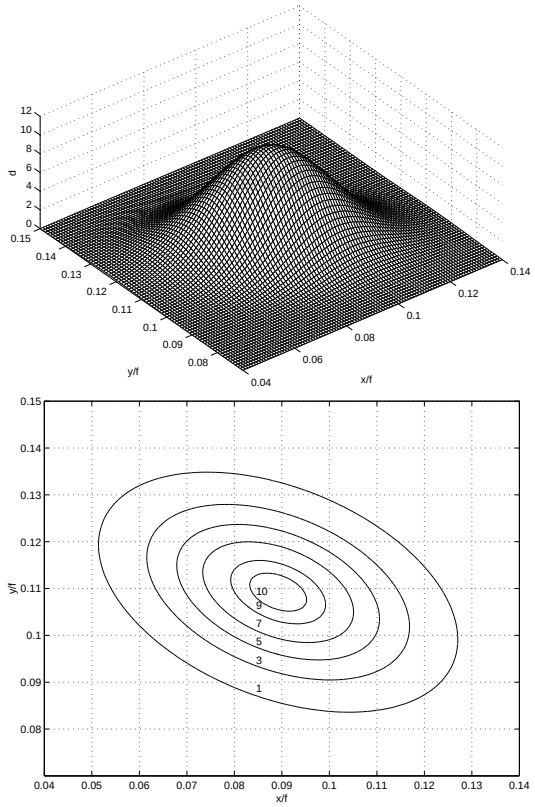

Figure 11. Projection of a flaw using a Gaussian model.

technique *splatting* outlined in Section 1 does not have this characteristic because the projected flaw corresponds to a smooth profile as shown in Figure 11. For this reason, splatting should only be used as a visualization technique and not as a method that simulates projections of round flaws.

We investigate now how region $\mathbf{F}$ is projected into the radioscopic image. As shown in Figure 2 there are two 2D coordinate systems: in the first one, the projection coordinate system (x, y), it take places a perspective projection without any distortion of the 3D object under test; in the second one, the image coordinate system (u, v), the image is deformed due to the distortion introduced by the image intensifier. Additionally, the coordinates are affected by rotation, translation and scaling. The relationship between these coordinate systems is given by the nonlinear function $\mathbf{f}$ and its inverse $\mathbf{g}$ as illustrated in Figure 12. The transformed pixels in image coordinate system are denoted by $(u, v) \in \mathbf{G}$. They are obtained form condition (24), that defines region $\mathbf{F}$, by computing $\bar{\mathbf{m}}$ as a function of $\mathbf{u} = [u\ v\ 1]^\mathsf{T}$. From (18) we have $\mathbf{m} = \mathbf{g}(\mathbf{u})$. By multiplying $\mathbf{m}$ with a 3×3 diagonal matrix and $\mathbf{K}$ where $K_{11} = K_{22} = 1/f$ and $K_{33} = 1$, it yields $\bar{\mathbf{m}} = \mathbf{K}\mathbf{m}$. Thus, substituting $\bar{\mathbf{m}} = \mathbf{K}\mathbf{g}(\mathbf{u})$ in condition (24) we obtain the definition of region $\mathbf{G}$ in the image coordinate system:

$$[\mathbf{g}(\mathbf{u})]^\mathsf{T}\mathbf{K}^\mathsf{T}\mathbf{\Lambda}\mathbf{K}\mathbf{g}(\mathbf{u}) > 0 \tag{29}$$

Since $\mathbf{g}$ is nonlinear the resulting boundary of $\mathbf{G}$ corresponds to a deformed ellipse.

If we evaluate (29) for each pixel of the radioscopic image the computing time of the flaw simulation increases considerably. However, due to the typical small size of flaws in comparison with the entire image size, a better performance of the algorithm can be obtained if condition (29) is only evaluated in the reduced area $\mathbf{Q}$ that encloses $\mathbf{G}$ as illusttated in Figure 12. Region $\mathbf{Q}$ is defined in $u_{min} \leq u \leq u_{max}$ and $v_{min} \leq u \leq v_{max}$. In following we describe how these bounds are calculated.

Firstly, we compute the points m_1, m_2, m_3, m_4 as the extremal points of the ellipse in projection coordinate system (see Figure 12). Using (26), (27) and (28) we obtain:

$$\mathbf{m}_i = \begin{bmatrix} x_i \\ y_i \\ 1 \end{bmatrix} = \begin{bmatrix} \cos(\alpha) & -\sin(\alpha) & x_0 \\ \sin(\alpha) & \cos(\alpha) & y_0 \\ 0 & 0 & 1 \end{bmatrix} \mathbf{r}_i, \tag{30}$$

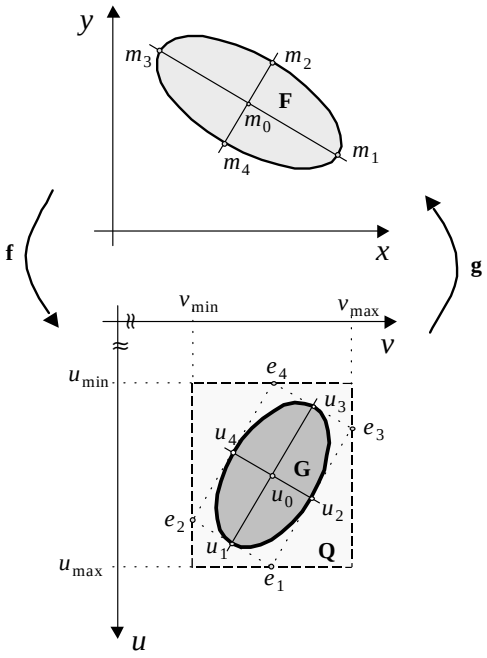

Figure 12. Projected ellipsoid in projection and image coordinate systems.

for $i = 0, ..., 4$, with $\mathbf{r}_0 = (0, 0, 1)^\mathsf{T}$, $\mathbf{r}_1 = (a_e, 0, 1)^\mathsf{T}$, $\mathbf{r}_2 = (0, b_e, 1)^\mathsf{T}$, $\mathbf{r}_3 = (-a_e, 0, 1)^\mathsf{T}$, and $\mathbf{r}_4 = (0, -b_e, 1)^\mathsf{T}$.

Secondly, the points m_i are transformed into image coordinate systems by $\mathbf{u}_i = \mathbf{f}(\mathbf{m}_i)$.

Thirdly, the vertices e_i of the polygon that encloses the deformed ellipse are computed as:

$$\begin{array}{ll} \mathbf{e}_1 = \mathbf{u}_1 + \mathbf{u}_2 - \mathbf{u}_0 & \mathbf{e}_3 = \mathbf{u}_3 + \mathbf{u}_2 - \mathbf{u}_0 \\ \mathbf{e}_2 = \mathbf{u}_1 + \mathbf{u}_4 - \mathbf{u}_0 & \mathbf{e}_4 = \mathbf{u}_3 + \mathbf{u}_4 - \mathbf{u}_0 \end{array} \quad (31)$$

Finally, the bounds of $\mathbf{Q}$ are computed by

$$\begin{array}{rcl} u_{min} & = & \text{fix}[\min(e_1(1), e_2(1), e_3(1), e_4(1))] \\ u_{max} & = & \text{fix}[\max(e_1(1), e_2(1), e_3(1), e_4(1)) + 1] \\ v_{min} & = & \text{fix}[\min(e_1(2), e_2(2), e_3(2), e_4(2))] \\ v_{max} & = & \text{fix}[\max(e_1(2), e_2(2), e_3(2), e_4(2)) + 1] \end{array}, \quad (32)$$

where the function $b = \text{fix}(a)$ rounds a toward zero, resulting in an integer b. Additionally, we must check that the bounds may not lie outside of the radioscopic image.

The algorithm for flaw simulation is summarized in Figure 13. The objective of this algorithm is to change the gray values of a radioscopic image by superimposing the projection of an ellipsoidal flaw according to the attenuation law for x-rays.

1. Calibrate the x-ray imaging system by estimating the parameters of the mapping function 3D $\rightarrow$ 2D (focal length f, matrix $\mathbf{S}$ (see (9)), and by finding the transformation functions between projection and image coordinate systems ($\mathbf{f}$ and $\mathbf{g}$ as defined in (14) and (18) respectively).
2. Take the radioscopic image of the object under test in the desired position and store it in matrix $\mathbf{I}$.
3. Estimate the absorption coefficient μ of the casting according to the energy used by the x-ray source (see (2)), and find the maximal thickness observable in the radioscopic image x_{max}.
4. Define the size of the flaw (parameters a, b and c) and the location and orientation of the flaw in the casting (matrix $\mathbf{S}_e$).
5. Compute the 4×4 matrix $\mathbf{H} = [\mathbf{S}\mathbf{S}_e]^{-1}$, and calculate the 3×3 matrices $\mathbf{\Phi}$ and $\mathbf{\Lambda}$ from (23) and (22) respectively.
6. Find the coordinates of the center (x_0, y_0), the half-axes a_e and b_e and the orientation α of the projected ellipse (see Figure 9) from (26), (27) and (28).
7. Estimate the area where the projected ellipse is located in the radioscopic image (see Figure 12) by finding the bounds u_{min}, u_{max}, v_{min} and v_{max} from (30), (31) and (32).
8. For $u = u_{min}, ..., u_{max}$ and for $v = v_{min}, ..., v_{max}$:
   - calculate $\mathbf{m} = \mathbf{g}(\mathbf{u})$, with $\mathbf{u} = [u\ v\ 1]^\mathsf{T}$ and $\mathbf{m} = [x\ y\ 1]^\mathsf{T}$,
   - compute $p = \bar{\mathbf{m}}^\mathsf{T}\mathbf{\Lambda}\bar{\mathbf{m}}$, with $\bar{\mathbf{m}} = [x/f\ \ y/f\ \ 1]^\mathsf{T}$,
   - if $p > 0$ then compute the length d of the intersection between x-ray beam and ellipsoid given by equation (21), and change the original gray value of the pixel (u, v) according to (6):

     $$I(u, v) := (I(u, v) - B)e^{\mu d} + B,$$

     where B is defined in (8).

Figure 13. Algorithm for flaw simulation.

5 Experimental Results

In this Section results of simulation of flaws in cast aluminum wheels using the approach outlined in the previous Section are presented. The dimensions of the wheels used in our experiments were 48 cm diameter and 20 cm height approximately. The focal length (distance between x-ray source and entrance screen of the image intensifier) was 90cm. The projection model of the x-ray imaging system was calibrated using a hyperbolic model [15, 14].

Figures 14, 15, 16 and 17 show the resulting radioscopic

Image No.	E [keV]	μ [1/cm]	x_{max} [cm]	a [mm]	b [mm]	c [mm]
1	54	0.8426	4.0	8	2	4
2	58	0.7569	3.8	4	2	1.5
3	50	0.9500	4.5	4	2	1.7
4	57	0.7765	3.85	6	3	2.5

Table 1. Values used in the simulations.

images for various simulated flaws. The values used to simulate the flaws in each image are summarized in Table 1.

Each image shows a real flaw and a simulated flaw. It was shown that the simulation results are almost identical with the real flaws. In Figure 18 a 3D plot of the gray values in the vicinity of the flaws shown in Figure 17 is illustrated. Due to the irregularity of the gray values of the simulated flaw, it can be seem that both real and simulated flaw shows similar patterns.

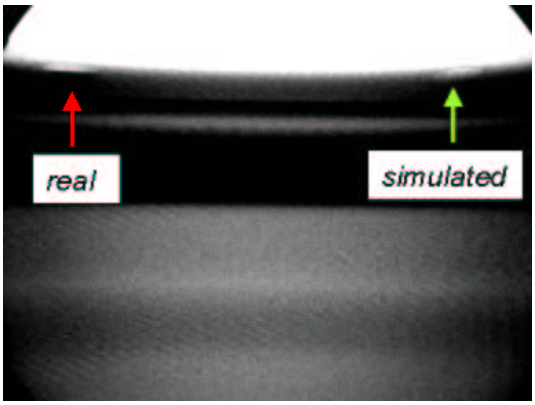

Figure 14. Radioscopic image 1.

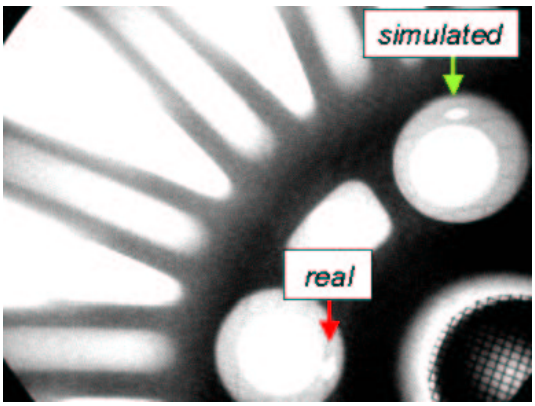

Figure 15. Radioscopic image 2.

6 Summary

A new method for the simulation of defects in radioscopic images of aluminum castings has been presented.

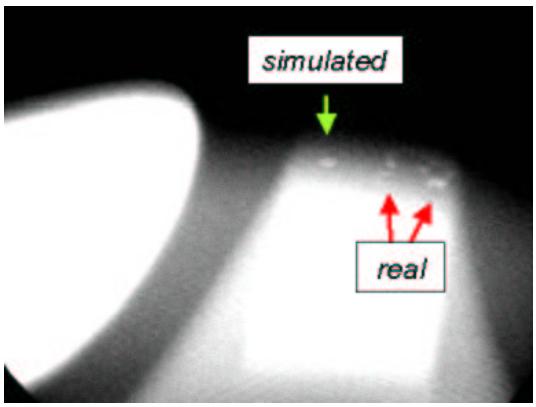

Figure 16. Radioscopic image 3.

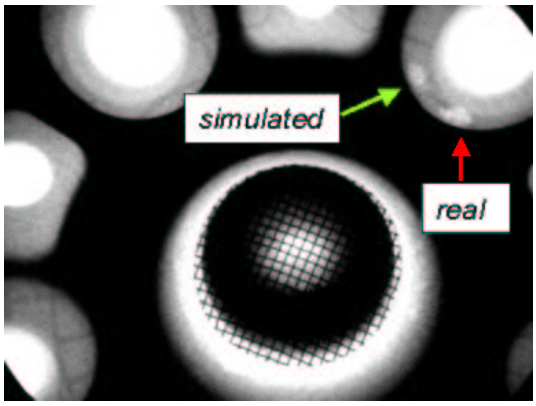

Figure 17. Radioscopic image 4.

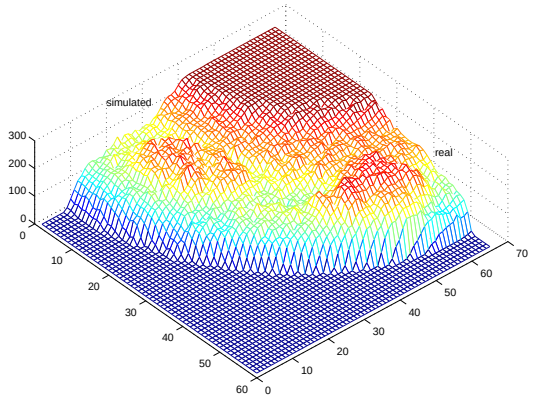

Figure 18. 3D plot of the gray values in the vicinity of flaws of Figure 17.

We propose an approach that simulates the flaws using a 3D ellipsoidal model, which is projected and superimposed onto real radioscopic images. The x-ray imaging process and the projection of a 3D object is discussed.

Using this tool a simulation of an ellipsoidal flaw of any size and orientation can be done in any position of the casting. This allows the precise evaluation of the performance of defect inspection systems in cases where the detection is known to be difficult.

The algorithm outlined in this paper can be used in other similar inspection processes. For instance, in the automated visual inspection of glass bottles in which the images of the bottles under test are taken against the light. In this examination process, the light is attenuated by glass in a similar manner as x-rays by aluminum castings.

The experimental results by simulating 3D flaws as ellipsoidal cavities has shown that the simulated defects are almost identical with the real flaws. However, to simulate other complex flaws, like cracks, a different 3D model must be used to calculate d.

Acknowledgments

I am grateful to Prof. Dr.-Ing. D. Filbert of the Technical University of Berlin for his contribution to this research. The radioscopic material of this paper was obtained with the help of Dr. Bavendiek and Dr. J.-M. Kosanetzky of YXLON International X-Ray GmbH (Hamburg) and Dr. rer.nat. U. Ewert of the Federal Institute for Materials Research and Testing (BAM, Berlin), and I wish to thank them. I would like to thank the three anonymous reviewers for valuable comments, in special the first one who gave me reference [20]. Finally, I am grateful to Mrs. A.M. Quiroz and Dr. F. Rannou for their suggestions.

References

[1] H. Boerner and H. Strecker. Automated x-ray inspection of aluminum casting. *IEEE Trans. Pattern Analysis and Machine Intelligence*, 10(1):79–91, 1988.

[2] C. Brack, H. Götte, F. Gossé, J. Moctezuma, M. Roth, and A. Schweikard. Towards accurate x-ray-camera calibration in computer-assisted robotic surgery. In *Proc. Int. Symp. Computer Assisted Radiology (CAR)*, pages 721–728, Paris, 1996.

[3] I. Bronstein and K. Semendjajew. *Taschenbuch der Mathematik*. Harri Deutsch, Thun-Frankfurt, Main, 24 edition, 1989.

[4] O. Faugeras, Q.-T. Luong, and T. Papadopoulo. *The Geometry of Multiple Images: The Laws That Govern the Formation of Multiple Images of a Scene and Some of Their Applications*. The MIT Press, Cambridge MA, London, 2001.

[5] D. Filbert, R. Klatte, W. Heinrich, and M. Purschke. Computer aided inspection of castings. In *IEEE-IAS Annual Meeting*, pages 1087–1095, Atlanta, USA, 1987.

[6] N. Freud, P. Duvauchelle, and D. Babot. Simulation of x-ray NDT imaging techniques. In *Proceedings of the 15th World Conference on Non-Destructive Testing (*15^{th}*–WCNDT)*, Rome, Oct. 15-21 2000.

[7] H. Haken and H. Wolf. *The Physics of Atoms and Quanta: Introduction to Experiments and Theory*. Springer, Berlin, Heidelberg, 5 edition, 1996.

[8] R. Halmshaw. *Non-Destructive-Testing*. Edward Arnold, London, 2 edition, 1991.

[9] R. I. Hartley and A. Zisserman. *Multiple View Geometry in Computer Vision*. Cambridge University Press, 2000.

[10] H. Hecker. *A new Method to Process X-Ray Images in the Automated Inspection of Castings*. PhD thesis, Institute for Measurement and Automation, Faculty of Electrical Engineering, Technical University of Berlin, 1995. (in German).

[11] W. Heinrich. *Automated Inspection of Castings using X-Ray Testing*. PhD thesis, Institute for Measurement and Automation, Faculty of Electrical Engineering, Technical University of Berlin, 1988. (in German).

[12] J.-M. Kosanetzky and H. Putzbach. Modern x-ray inspection in the automotive industry. In *Proc. 14th World Conference of NDT (*14^{th}*–WCNDT)*, New Delhi, Dec. 8-13 1996.

[13] H. Kuchling. *Taschenbuch der Physik*. Harri Deutsch, Thun-Frankfurt, Main, 12 edition, 1989.

[14] D. Mery. *Automated Flaw Detection in Castings from Digital Radioscopic Image Sequences*. Verlag Dr. Köster, Berlin, 2001. (Ph.D. Thesis in German).

[15] D. Mery and D. Filbert. The epipolar geometry in the radioscopy: Theory and application. *at - Automatisierungstechnik*, 48(12):588–596, 2000. (in German).

[16] D. Mery, T. Jaeger, and D. Filbert. Automated quality control of castings – state of the art. *tm - Technisches Messen*, 68(7-8), 2001. (in German).

[17] G. Ogiermann and G. Mann. *Catalog of Casting Defects*. German Society of Nondestructive Testing, Oberursel, 1979.

[18] G.-R. Tillack, C. Nockemann, and C. Bellon. X-ray modelling for industrial applications. *NDT & E International*, 33(1):481–488, 2000.

[19] J. Weng, P. Cohen, and M. Herniou. Camera calibration with distorsion models and accuracy evaluation. *IEEE Trans. Pattern Analysis and Machine Intelligence*, 4(10):965–980, 1992.

[20] L. Westover. Footprint evaluation for volume rendering. *Proceedings of SIGGRAPH*, 24(4):367–376, 1990.